Seal types of water-entry cavities generated by the impact of spheres with decreasing Bond number

Yuxue Zhong[1,2], Yan Du[1,2], Rundi Qiu[1,3], Zhijian Xiao[1,2], Jian Huang[1,2], Zhiying Wang[1], Jingzhu Wang[1,2*], and Yiwei Wang[1,2,3]

[1] *Key Laboratory for Mechanics in Fluid Solid Coupling Systems, Institute of Mechanics, Chinese Academy of Sciences, Beijing 100190, China;*
[2] *School of Engineering Science, University of Chinese Academy of Sciences, Beijing 100049, China;*
[3] *School of Future Technology, University of Chinese Academy of Sciences, Beijing 100049, China*

The evolution of water-entry cavities gives rise to interesting dynamic phenomena that occur in nature and engineering fields. The evolution and seal types of the cavities remain unsettled at Bo less than 10^{-2} since it is difficult to propel a small sphere to impact a water surface at high speed. In the present study, an experiment based on the laserdriven principle is conducted to accelerate a small sphere to hundreds m/s. The types of cavity seal are classified as quasi-static, shallow seal, deep seal, and surface seal within a Bo range of $1-7.57 \times 10^{-2}$. The transition mechanism from a shallow seal to a deep seal is investigated by analyzing the cross-sectional characteristics of cavity necks. With a further decrease in Bo ($5.69 \times 10^{-2} - 8.41 \times 10^{-3}$), the shallow seal is changed directly to a surface seal since the pinch-off time of the cross section at the cavity neck decreases with Bo, and hence, the deep seal disappears. Finally, a parameter study is conducted by varying We and Bo in the air cavity. Two boundaries are obtained: $We \approx 64$ for the transition between quasi-static and shallow seals and $We \approx 326$ for the transition between shallow seals and surface seals.

Air cavity, Seal types, Laser-driven method, Shallow seal, Deep seal

1. Introduction

The water-entry problem has been widely considered in engineering fields [1-4] and nature [5,6]. An air cavity is generated when a projectile enters water or another liquid. Four types of cavities have been classified, i.e., (1) quasi-static, (2) shallow seal, (3) deep seal, and (4) surface seal, according to the seal positions and time. The present study focuses on the behaviors of a deep seal cavity, which is characterized by the first pinch-off event occurring much closer to the sphere, typically one-third to one-half of the distance between the sphere and the undisturbed free surface. The main dimensionless parameters affecting its dynamics are the Bond number (Bo) and the Froude number (Fr).

At a high Bo ($Bo \gg 1$), the seal types are classified into quasi-static, deep, and surface seals. Glasheen and McMahon [7] investigated the dynamics of the deep seal of cavity-induced disk impacts into water at a high Bo (10^3) and defined a dimensionless pinch-off time of the cavity. Lee et al. [8] numerically investigated the mechanism of the water-entry cavity formed by sphere impact at a high Bo and found that both the dimensionless time and the position of the deep seal are independent of Fr. Bergmann et al. [9] analyzed the pinch-off behaviors of a cylindrical cavity at $Bo \approx 125$ and found that the collapses of the cavity were not self-similar. Duclaux et al. [10] experimentally studied the dynamic characteristics of a water-entry cavity and derived an approximate analytical model for describing the evolution of the cavity. Grumstrup et al. [11] experimentally observed the volume oscillations of the cavities after a deep seal occurred.

Gekle et al. [12] found that the dimensionless pinch-off time retains different power-law dependences on *Fr* due to capillary waves created when a submerging object passes the water surface. Truscott and Teche [13] found that the dimensionless pinch-off time of a deep seal was not affected by the spin of the sphere. Aristoff et al. [14] characterized both the deceleration rate and resulting change in the associated water-entry cavities by examining low-density spheres that decelerated substantially following impact. Jiang et al. [15] performed water entry experiments of a constraint posture projectile under different entry angles and ventilation rates. Yang et al. [16] studied the influences of the air, the cavity body mass, the cavity body size, and the incline angle on the dynamic characteristics of the water-entry cavity body.

The near water surface cavity flow characteristics, including splash sheet, surface closure, pull away, deep collapse and cavity ripples, were investigated under different entry angles and ventilation rates without the posture perturbation influence of the projectile.

The types of the cavity seal are affected remarkably by the values of *Fr* at low *Bo* values. Compared with that at high *Bo* values, the shallow sealing of a cavity occurs as a unique phenomenon at low *Bo* values, which is characterized by the presence of capillary waves on the wall of the cavity occurring relatively close to the free surface. At a low *Fr*, the conditions under which the projectile sink, bounce off, or oscillate upon impact with water have also been investigated via numerical and experimental approaches [17-20]. A large value of *Fr* leads to a large cavity after a projectile impacts the water surface. It is difficult to perform an experiment for generating a high impact velocity of the projectile at low *Bo*. Recently, hydrophobic spheres have been used to generate a large cavity in water-entry experiments since a hydrophobic coating decreases the critical velocity at which the three-phase contact line becomes unstable, and hence, the sphere is wrapped by an air layer at a low impact velocity.

Duez et al. [21] found that the threshold impact velocity for producing a large cavity is a function of the static contact angle of the impacting body, and the critical velocity of hydrophilic spheres is higher than that of hydrophobic spheres. Aristoff and Bush [22] presented the results of a combined experimental and theoretical investigation of the normal impact of hydrophobic spheres on a water surface. Their parametric study revealed four distinct cavity types that arise as a function of *Fr*: quasi-static seal, shallow seal, deep seal, and surface seal. Li et al. [23] studied the effect of Reynolds number on drag reduction of superhydrophobic surface. Ding et al. [24] investigated cavity formation during the impact of spheres and cylinders into a liquid pool by using a combination of experiments, simulations, and theoretical analysis, with particular interest in contact-line pinning and its relation to subsequent cavity evolution.

Huang et al. [25] experimentally obtained the cavity behaviors and motion of water entry of small superhydrophobic spheres with a radius of 0.175–10 mm and derived the nondimensional relationship between the floating oscillation and sinking behaviors of the sphere. Choi et al. [26] investigated the effect of continuous-wave laser irradiation on the cavity evolution behind a sphere in water entry. The radius and impact velocity of the sphere were changed, by which both shallow and deep seals were considered. Guleria et al. [27] experimentally analyzed the trajectory of a sphere, the dynamics of the cavity, and the formation of the Worthington jet at $Bo \sim 10^{-1}$. Yoo et al. [28] carried out three-dimensional numerical simulations of the water-entry problem and investigated the behaviors of spheres with different wetting characteristics. Based on the abovementioned studies, the seal types and bubble dynamics of the cavity have been widely analyzed at a high *Bo* value (10^{-1}–10^{0}). Given the study by Aristoff and Bush [22], surface tension becomes dominant with regard to the bubble dynamics with a further decrease in *Bo*. Li et al. [29] also found that the surface tension gradient is very important for the interfacial flow around the bubble. This brings different mechanisms and physical phenomena of the cavity seal.

In the present study, an experiment based on the laser-driven principle is conducted to accelerate a small sphere to hundreds of meters per second. The seal types of the air cavity are observed when the ranges of Weber number (*We*) and *Bo* are 10–10^{3} and 10^{-2}–10^{-3}, respectively. Subsequently, the transition mechanism from a shallow seal to a deep seal is investigated by obtaining the characteristics of the spheres and the cavity cross section at the neck close to the free surface. Finally, a parametric study is conducted by varying *We* and *Bo*. Deep seals disappear and are replaced by shallow seals within the range of *Bo* (5.69×10^{-2}–8.41×10^{-3}).

2.   Experimental setup

To observe the behaviors of the air cavity induced by the high-speed impact of spheres, an experiment is carried out based on the laser-driven method. As shown in Fig. 1a, a pulse laser with a wavelength of 532 nm (MQU-700-III, Beijing. ZK Laser Co., Ltd.) is focused on the position of an aluminum film attached to the reverse side of a water tank cover by a concave mirror (f_R = 15.24 mm, $A_{\text{off-axis}}$ = 90°). The dimensions of the water tank are 80 mm in length, 80 mm in width and 100 mm in depth, and the thickness of the K9-glass-made cover is 5 mm. A high-pressure plasma is generated between the cover and the aluminum film, which leads to the deformation of the aluminum film, as shown in Fig. 1b. Meanwhile, a sphere attached to the other side of the aluminum film is driven to impact the water surface at a high speed, inducing an air cavity, as shown in

Fig. 1b. A high-speed camera (Phantom v1612, Vision Research) with a micron-sized lens (Canon, MP-E65 mm f/2.8 1-5×) begins to record the dynamics of the cavity at sampling frequencies of 16000 to 24000 fps when the pulse laser is triggered. A white light source (CLL-4800TDX) is placed on the opposite side of the tank. In the experiments, a stainless-steel sphere is used, and its density ρ_s is 7850 kg/m^3. The sphere radii R_0 are 0.25 mm, 0.3 mm, 0.5 mm, 0.6 mm, 0.65 mm, and 0.75 mm. The impact velocities U_0 range from 1 m/s to 10 m/s by adjusting the laser energy. Here U_0 is obtained by the ratio of the distance of sphere movement between the first two frames to the time interval just after the sphere impacts. The ranges of Bo, We, and Fr are shown in Table 1.

3.   Results and discussion

It is difficult to drive a sphere with a low Bo to impact a water surface at high speed, and the seal types of the air cavities remain unsettled at Bo values lower than 10^{-2}. In the present study, small spheres can be accelerated to hundreds of meters per second based on the laser-driven method. The seal types of the cavities are observed when the Bo ranges from 10^{-2}–10^{-3}. Seal types are classified into four types, namely, quasi-static, shallow, deep, and surface seals, at

Table 1   Main affecting dimensionless parameters in the present study

Parameter	Symbol	Definition	Order of magnitude
Bond number	Bo	$\rho g R_0^2 / \sigma$	10^{-3}–10^{-2}
Weber number	We	$\rho U_0^2 R_0 / \sigma$	10^1–10^3
Froude number	Fr	$U_0^2 / (g R_0)$	10^3–10^4

$Bo = 1$–7.57×10^{-2}. With a further decrease in Bo, the deep seal disappears at $Bo = 5.69 \times 10^{-2}$–8.41×10^{-3}. Thus, the mechanism for the disappearance of the deep seal is investigated by comparing the closure time of the cavity at the shallow neck between deep seal and shallow seal. It is because the deep seal is replaced by the shallow seal instead of the surface seal with the decrease of Bo. The phenomenon is also predicted theoretically by Aristoff and Bush [22].

3.1   Four types of cavities within a Bo range of 1–7.57× 10^{-2}

The initial energy of cavity formation can be obtained from the impact of a sphere on a water surface. As the sphere is completely immersed and sinks in water, an air cavity forms, expands, shrinks, and pinches. For the impact of spheres at $Bo = 1$–7.57×10^{-2}, we observe four distinct cavity types, i.e., (1) quasi-static, (2) shallow seal, (3) deep seal, and (4) surface seal, with increasing impact velocity U_0, as shown in Fig. 2. U_0 is obtained by measuring the distance of the
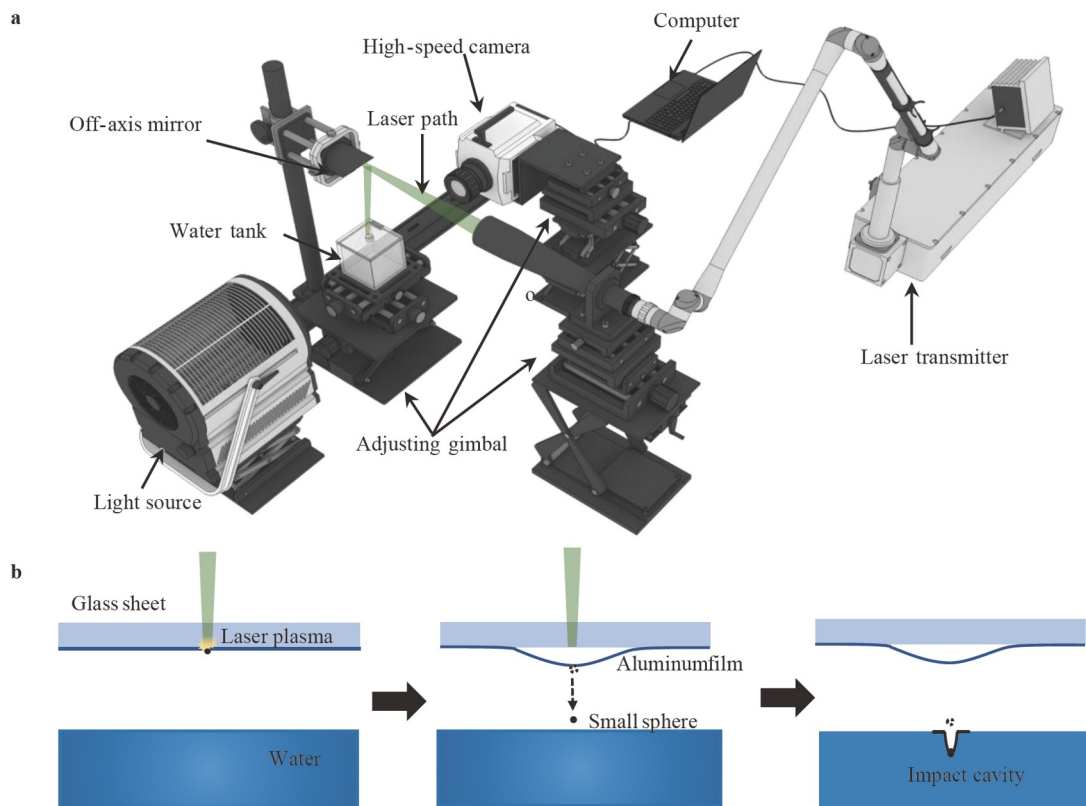

Figure 1   **a** Schematic of the experimental setup for observing the behaviors of the air cavity induced by sphere impact on a water surface at low Bo; **b** mechanism of the laser-driven method for the high-speed impact of the sphere.
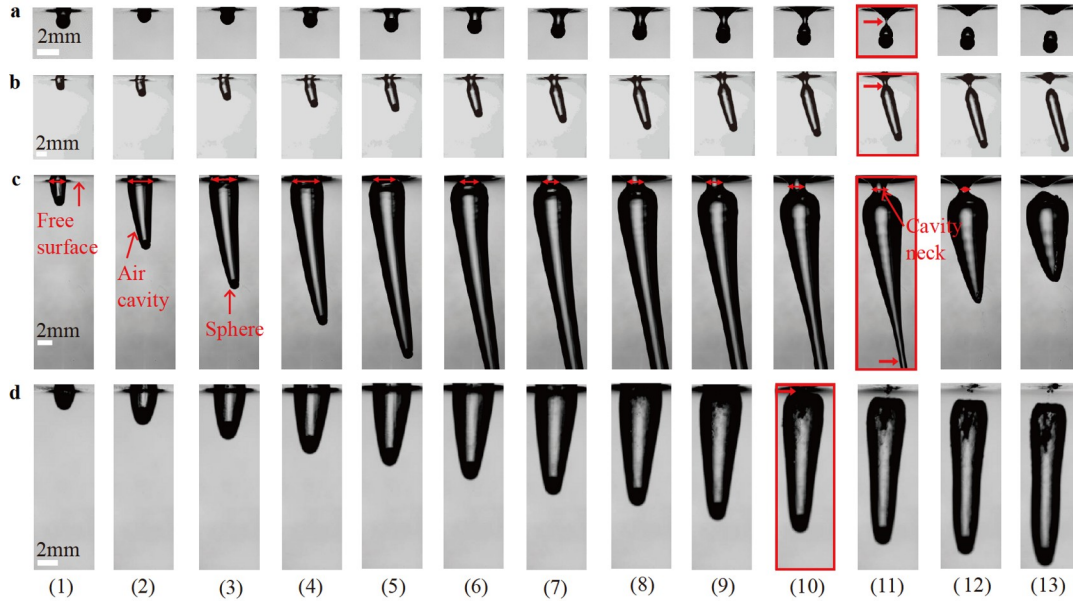
Figure 2 Four seal types of the cavities induced by the water entry of an $R_0 = 0.75$ mm sphere ($Bo = 7.57 \times 10^{-2}$) with increasing impact velocity U_0: **a** quasi-static seal, **b** shallow seal, **c** deep seal, and **d** surface seal. The initial impact velocities of sphere U_0 and the time intervals between sequential images Δt are 1.12 m/s and 0.25 ms for case **a**, 2.02 m/s and 0.25 ms for case **b**, 5.25 m/s and 1.437 ms for case **c**, and 8.51 m/s and 0.125 ms for case **d**, respectively. The red box in the images highlights the occurrence of the first pinch-off of the cavity. The red double arrows indicate the evolution of the cross section of the cavity at the neck.

sphere movement at the time interval between the first two frames just after the sphere enters the water. The radius of the sphere R_0 and corresponding Bo are 0.75 mm and 7.57×10^{-2}, respectively. For quasi-static conditions, air entrainment is minimal, and hence, only a minute bubble remained attached to the sphere after the cavity pinches approximately at the position of its neck. As U_0 increases, the cavity of the shallow seal occurs, and the pinch-off position is similar to that of the quasi-static position. The difference between the two seals is the air volume entrained by the sphere after pinch-off. The air volume is much larger for the shallow seal but comparable to the sphere for the quasi-static seal. A further increase in U_0 gives rise to the cavity of the deep seal, as shown in Fig. 2c. High-speed impact induces a comparably substantial air cavity. The cavity expands as the sphere sinks. The cavity shrinks both at the neck and at a greater depth. The middle part of the cavity forms the shape of a cone with further shrinkage just before pinch-off. Eventually, pinch-off first occurs at a greater depth (see frame (11) in Fig. 2c). Subsequently, the cavity immediately pinches at the neck (see frame (13) in Fig. 2c). At the highest U_0, a cavity of surface seal is observed and characterized by the pinch-off of the cavity at the free surface with a long cavity attached to the sphere below. Although the vertical water entry of the sphere is not generated perfectly in some cases, it is thought not to influence the seal types of the cavity.

The distinctive difference between shallow and deep seals is the position where the cavity first pinches. Consequently, the seal type of the cavity transitions from a shallow seal to a

deep seal cavity when the pinch-off time of the cross section at the cavity neck t_{sn} increases, so pinch-off first occurs at a greater depth. We compare the evolution of the cross section and the dimensionless pinch-off time at the cavity neck in the cases of shallow seals and deep seals, as shown in Fig. 3. The ordinate and abscissa are the dimensionless radius of cross section r/R_0 and time tU_0/R_0, respectively. After the sphere enters the water, the air cavity expands, shrinks, and pinches. The expanding velocity and the maximum radius of the cross section at the cavity neck increase with U_0.

To clarify how the impact velocity affects the expanding velocity and maximum radius of the cavity, we investigate the deceleration of the sphere in water, and its mean velocity is defined as H/t when it moves to a depth H at time t. In Fig. 4, the abscissa is the dimensionless time t/t_{sn}. t_{sn} is the pinch-off time of the cross section at the cavity neck. The dimensionless mean velocities decrease exponentially at $U_0 = 5.25$ m/s and decrease approximately linearly at $U_0 = 2.45$ m/s, 3.71 m/s, and 4.07 m/s. As the sphere descends, the sphere transfers momentum to the fluid by forcing it radially outward. Hence, the cavity in the case of deep seals obtains a high expanding velocity and maximum radius due to a greater deceleration of the sphere.

By the force analysis of the cross section at the cavity neck, the total pressure difference ΔP of the cross section is expressed by the surface tension, aerodynamic pressure, and hydrostatic pressure.

$$\Delta P = \sigma \nabla \cdot \mathbf{n} + C_a \rho U_{air}^2 + \rho g z_p, \quad (1)$$

where σ is the surface tension coefficient. Figure 5 shows a

schematic of a water-entry cavity. The sphere of radius R_0 enters the water vertically. At time t, the sphere reaches the depth of $z = H$, and the depth of the shallow neck is z_p. This cavity can be represented by $r(z,t)$. r_z is $\partial r / \partial z$ and r_{zz} is $\partial^2 r / \partial z^2$. Because the angle between the cavity wall and the z-axis is very small, r_z and r_{zz} can be ignored in the present study. The normal gradient of the cavity wall $\nabla \cdot \mathbf{n} = \left(1 + r_z^2/r - r_{zz}\right)/\left(1 + r_z^2\right)^{2/3}$ can be reduced to $1/r$ by assuming that the cavity walls have large slopes ($r_z \ll 1$)

Figure 3 Evolution of the dimensionless radius of the cross section at the cavity neck for $R_0 = 0.75$ mm. The ordinate and abscissa are r/R_0 and tU_0/R_0, respectively. The black squares, red circles, green upper triangles, and blue lower triangles indicate the results from initial velocities U_0 of 2.45 m/s, 3.71 m/s, 4.07 m/s, and 5.25 m/s, respectively. The dotted lines divide the expansion and contraction phases of the cavities. The dimensionless pinch-off times are 10.39, 26.38, 63.8, and 121.19 at $U_0 =$ 2.45 m/s, 3.71 m/s, 4.07 m/s, and 5.25 m/s, respectively. The sampling frequency of the high-speed camera is 16000 fps. The errors of the closure times are within one interval time of the sampling frequency.

Figure 4 Evolution of the dimensionless mean velocity of the sphere at different impact velocities U_0 of 2.45 m/s, 3.71 m/s, 4.07 m/s, and 5.25 m/s. The ordinate and abscissa are $(H/t)/U_0$ and tU_0/R_0, respectively. Here, the mean velocity of the sphere is defined as H/t when it moves to a depth H at time t.

and that the longitudinal component of the curvature is negligible ($r_{zz} \ll 1$). $C_a = 0.5$ is the aerodynamic pressure coefficient. U_{air} is the transient air velocity at the cavity section. According to Eshraghi et al. [30], the volumetric flow rate $Q(t)$ of air into the cavity is described by the time rate change in the cavity volume given by $Q(t) = dV_{cav}(t)/dt$, U_{air} is estimated by $U_{air} \approx Q(t)/(\pi r^2)$, where πr^2 is the area of the cavity section. z_p is the pinch-off depth of the shallow neck section.

Figure 6 shows the evolution of the dimensionless total pressure difference of the cross section at the cavity neck for different U_0 values. The ordinate and abscissa are the dimensionless total pressure difference $\Delta P/(\rho U_0^2)$ and time
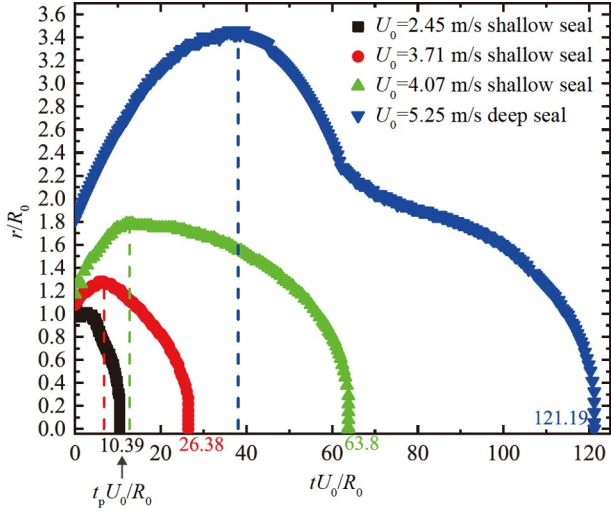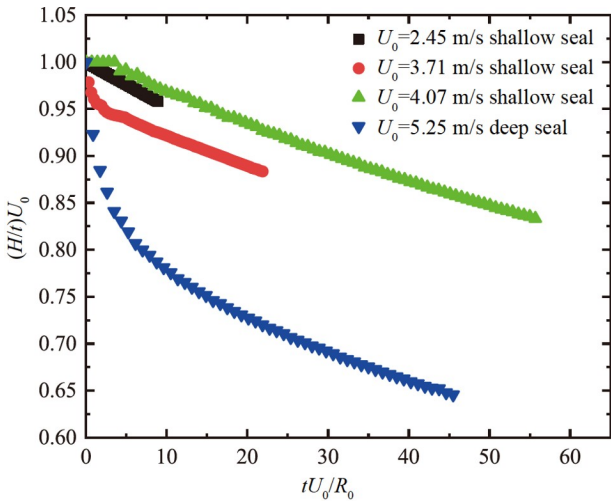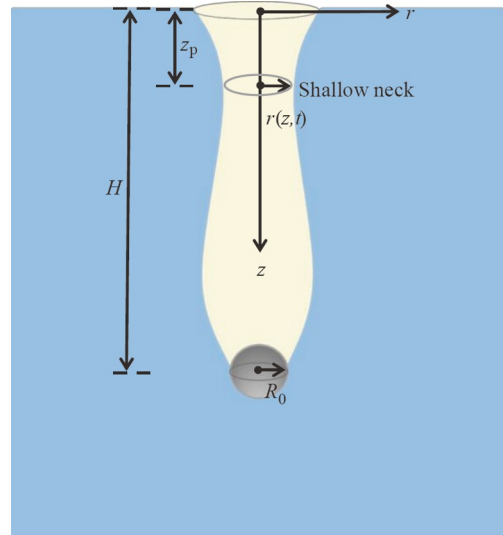

Figure 5 A schematic of a water-entry cavity.
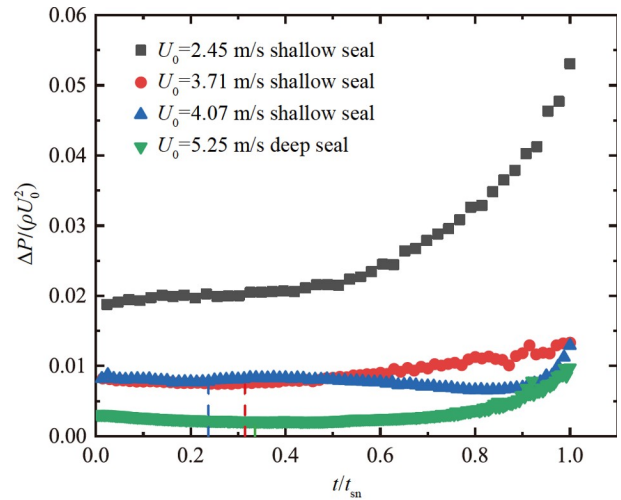

Figure 6 Evolution of the dimensionless total pressure difference ΔP of the cross section at the cavity neck for the $R_0 = 0.75$ mm cases. The ordinate and abscissa are $\Delta P/(\rho U_0^2)$ and t/t_{sn}, respectively. The black squares, red circles, blue upper triangles, and green lower triangles indicate the results from impact velocities U_0 of 2.45 m/s, 3.71 m/s, 4.07 m/s, and 5.25 m/s, respectively. The dotted lines divide the expansion and contraction phases of the cavities.

t/t_{sn}, respectively. The positive direction of the pressure difference is the shrinkage of the cavity. Consequently, the expansion is resisted, and the shrinkage of the cavity is accelerated under the action of such total pressure difference ΔP. From Fig. 6, it is found that the total pressure difference ΔP remains constant before the cavity contracts and increases during the shrinkage of the cavity in all cases. ΔP decreases with increasing U_0. This suggests that a lower resultant force resists the expansion and accelerates the shrinkage of the cavity at a higher U_0 value. Furthermore, the cavity obtains a greater amount of momentum from sphere deceleration. As a result, the pinch-off time t_{sn} increases with U_0, and the seal type is changed into a deep seal.

We investigate the evolution of component forces Δp in Eq. (1) at different U_0 values, as shown in Fig. 7. The black squares, red circles, blue triangles, and lower triangles indicate the total pressure difference, surface tension, aerodynamic pressure, and hydrostatic pressure, respectively. In Fig. 7a, the air cavity directly shrinks since enough energy

to expand is not obtained from the impact of the sphere on the water surface. With increasing U_0, the air cavity first expands and then shrinks. The surface tension is a dominant factor in expansion and shrinkage, and the actions of the hydrostatic pressure and aerodynamic pressure can be ignored. Furthermore, the surface tension decreases as U_0 increases. This is a main reason why the total pressure difference ΔP decreases as U_0 increases.

Figure 8 shows the dependence on *We* of the dimensionless pinch-off time $t_{sn}U_0/R_0$ of the cross section at the cavity neck. With increasing U_0, t_{sn} increases, and hence, the shallow seal transitions to a deep seal. $We \approx 125$ is the boundary between the shallow seal and deep seal.

3.2 Disappearance of the deep seal within a *Bo* range of 5.69×10^{-2}-8.41×10^{-2}

With a further decrease in *Bo*, the deep seal of the cavity disappears. The cavity types are classified into quasi-static
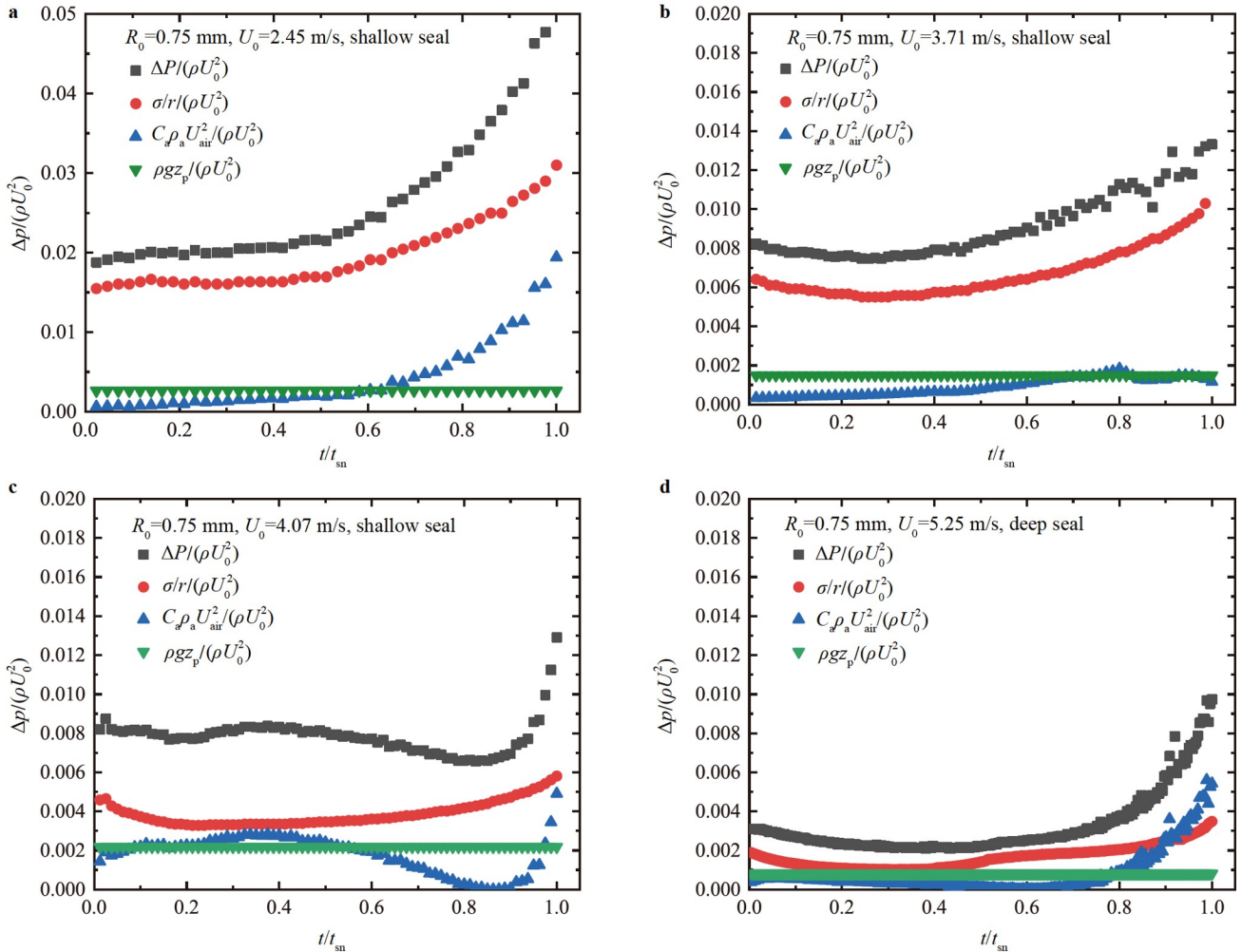

Figure 7 Evolutions of each force in Eq. (1) at different impact velocities U_0 of 2.45 m/s, 3.71 m/s, 4.07 m/s, and 5.25 m/s. The total pressure difference ΔP and the component forces Δp are nondimensionalized by ρU_0^2. The black squares, red circles, blue upper triangles, and green lower triangle denote the total pressure difference, surface tension, aerodynamic pressure, and hydrostatic pressure, respectively. The dotted lines divide the expansion and contraction of the cavities.
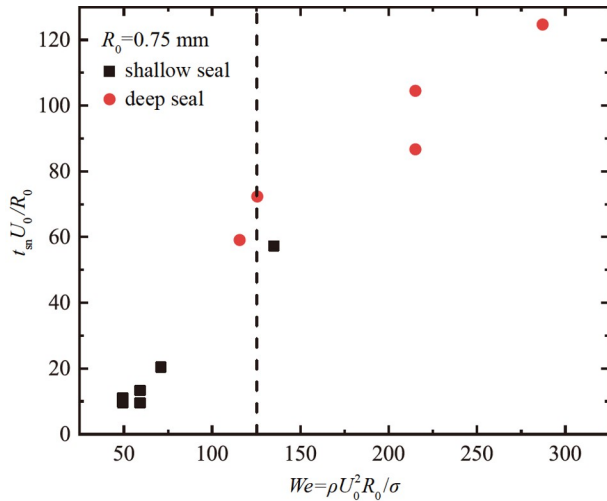
Figure 8 Dependence on We of the dimensionless pinch-off time $t_{sn}U_0/R_0$ of the cross section at the cavity neck for $Bo = 7.57 \times 10^{-2}$, corresponding to $R_0 = 0.75$ mm and $\rho_s = 7.8$ g/cm^{-3}. The cavity types of shallow seals and deep seals are denoted by black squares and red circles, respectively.

(Fig. 9a), shallow seal (Fig. 9b), and surface seal (Fig. 9c) with increasing U_0 at $R_0 = 0.6$ mm, as shown in Fig. 9. At $U_0 = 2.076$ m/s, the quasi-static of the cavity occurs and is characterized by a small air volume entrained by the sphere after pinch-off. Compared with the results in Fig. 2c, the cavity first pinches at the neck, rather than at a greater depth when U_0 increases to 5.22 m/s, as shown in Fig. 9b. A further increase in U_0 leads to the surface seal of the cavity. Subsequently, we investigate the mechanism of the disappearance of the deep seal for Bo values less than 7.57×10^{-2}.

First, the evolution of the cross-sectional radii at the

cavity neck is investigated at different R_0 values when U_0 is approximately equal to 5 m/s, as shown in Fig. 10a. The deep seals are not induced at $R_0 = 0.6$ mm and 0.65 mm and occur at $R_0 = 0.75$ mm (see Fig. 10b). The expanding velocities of the cavity cross section are almost the same. This means that the impact velocity U_0 is dominant for determining the expanding velocity. The values of the maximum radius of cross section r_{max} increase with R_0. Compared with the results in Fig. 3, the maximum radius depends on the combination of U_0 and R_0. As a result, the pinch-off time of the cross section at the cavity neck t_{sn} increases with R_0.

The decelerations of the sphere in water are investigated at different R_0 values, as shown in Fig. 11. We obtain similar phenomena to those in Fig. 4. The dimensionless mean velocities decrease rapidly as an exponential function at $R_0 = 0.75$ mm in the case of a deep seal but decrease slowly at $R_0 = 0.6$ and 0.65 mm in the cases of a shallow seal. As a result, the deceleration of the sphere slows with R_0. This indicates that a smaller sphere transfers less momentum to the fluid, and hence, a smaller maximum radius of the cross section is obtained.

Next, we investigate the pressure difference ΔP of the cross section at the cavity neck, as shown in Fig. 12. The dimensionless pressure difference increases with decreasing R_0. Consequently, a higher resultant force resists the expansion and accelerates the shrinkage of the cavity at a smaller R_0. Furthermore, the maximum radius of the cross section is smaller. As a result, the pinch-off time t_{sn} decreases with decreasing R_0 and the deep seals disappear
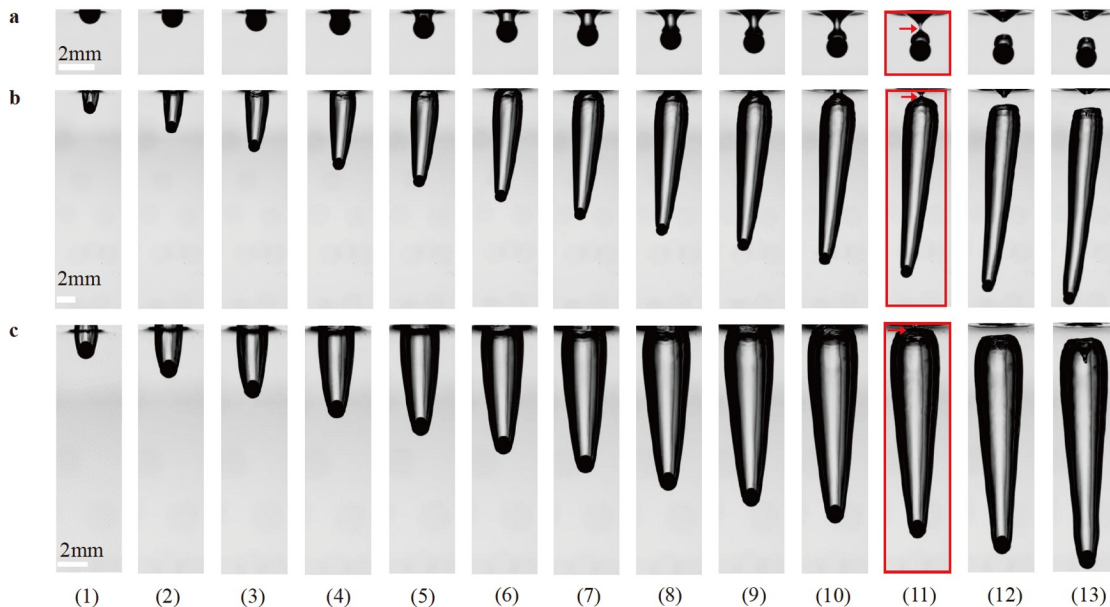

Figure 9 Three types of cavities induced by the water entry of the sphere at $R_0 = 0.6$ mm ($Bo = 4.85 \times 10^{-2}$) with increasing U_0: **a** quasi-static, **b** shallow seal, and **c** surface seal. The impact velocities of sphere U_0 and the time intervals between sequential images Δt are 2.08 m/s and 0.111 ms for case **a**, 5.22 m/s and 0.333 ms for case **b**, and 6.72 m/s and 0.222 ms for case **c**, respectively. The red box in the images highlights the occurrence of the first pinch-off of the cavity.
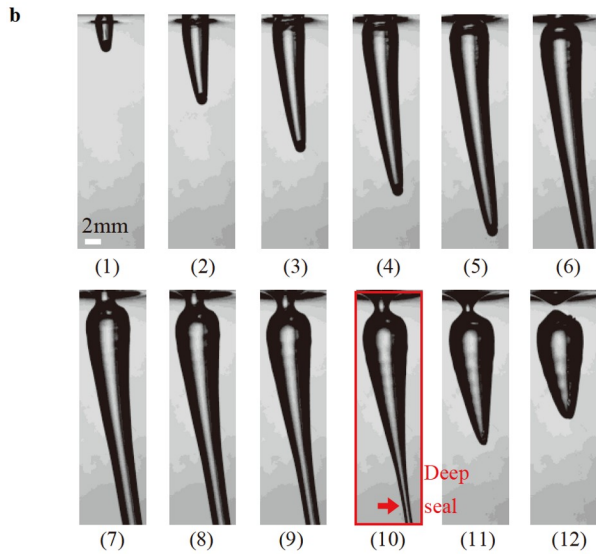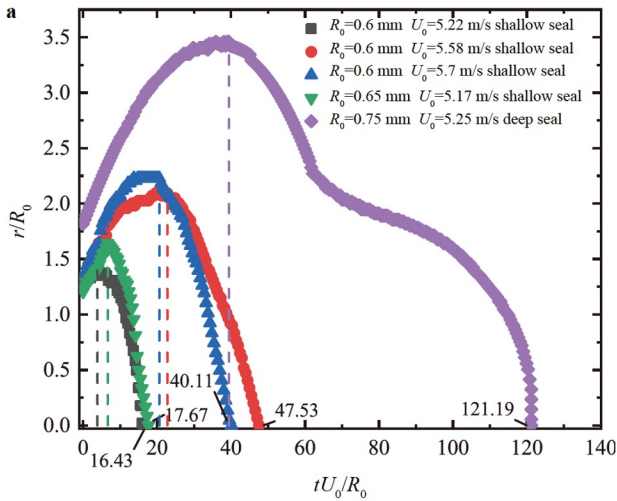
Figure 11 Evolution of the dimensionless mean velocity of the sphere at $U_0 \approx 5$ m/s for different radii of the spheres R_0. The ordinate and abscissa are $(H/t)/U_0$ and t/t_{sn}, respectively.

Figure 12 Evolution of the dimensionless pressure difference of the cross section at the cavity neck at $U_0 \approx 5$ m/s for different radii of the spheres R_0. The ordinate and abscissa are $\Delta p/(\rho U_0^2)$ and t/t_{sn}, respectively. The dotted lines divide the expansion and contraction of the cavities.

Figure 10 **a** Evolution of the dimensionless radius of the shallow neck cross section at $U_0 \approx 5$ m/s for different radii of the spheres R. The ordinate and abscissa are r/R_0 and tU_0/R_0, respectively. The dotted lines divide the expansion and contraction of the cavities. For the experimental conditions with $R_0 = 0.75$, 0.65, and 0.6 mm, the sampling frequencies of the camera are 16000 fps, 18000 fps, and 18000 fps, respectively. The errors of closure times are within one interval time of the sampling frequency. **b** Deep seal of the cavity at $R_0 = 0.75$ mm and $U_0 = 5.25$ m/s.

and are replaced by the shallow seal.

Figure 13 shows the evolution of each force in Eq. (1) at $U_0 \approx 5$ m/s for different radii of the spheres. A deep seal occurs at $R_0 = 0.75$ mm, and a shallow seal occurs at $R_0 = 0.65$ mm and 0.6 mm. Compared with the surface tension, the aerodynamic pressure increases largely with decreases in R_0, improving the action on the expansion and shrinkage of the cavity. Meanwhile, it is found that the action of aerodynamic pressure increases with decreasing R_0. As a result, the pressure difference ΔP increases as R_0 decreases.

A parametric study was conducted by varying the sphere radius and impact velocity, thus elucidating the influence of *We* and *Bo* on the air cavity (see Fig. 14). At $Bo = 7.57 \times 10^{-2}$,
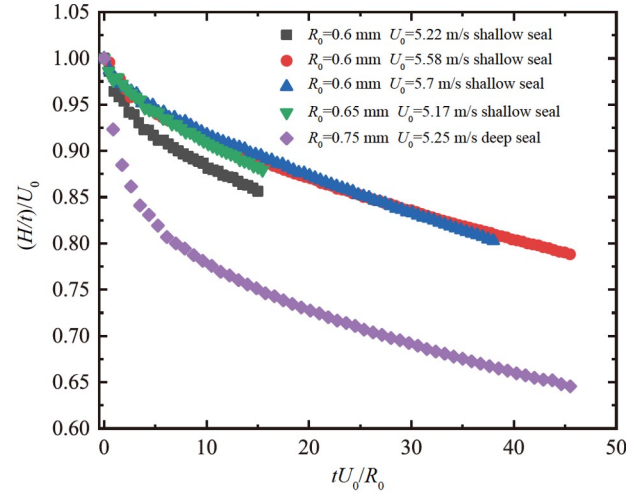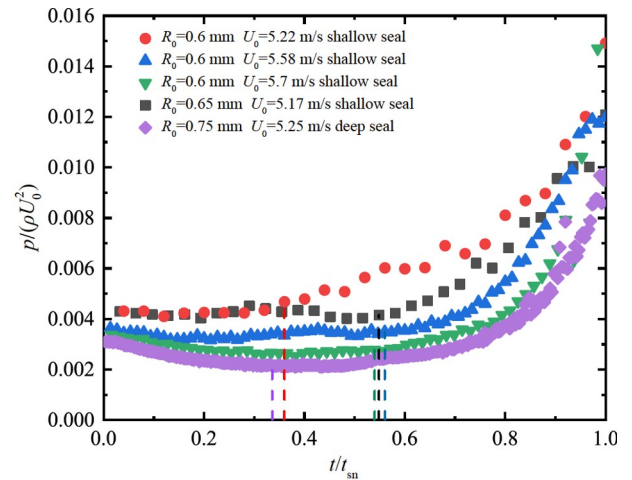
the cavity type transitions from quasi-static to shallow seal to deep seal to finally surface seal as *We* increases. At *Bo* values smaller than 7.57×10^{-2}, the shallow seal is changed directly to the surface seal, and the deep seal disappears. Furthermore, it is found that the shallow seal takes the place of the deep seal with a further decrease in *Bo*. Two boundaries are obtained, $We \approx 64$ for the transition between quasi-static and shallow seals and $We \approx 326$ for the transition between the shallow seal and surface seal.

4. Conclusions

We experimentally investigated the seal types of air cavities induced by the impact of spheres on the water surface with
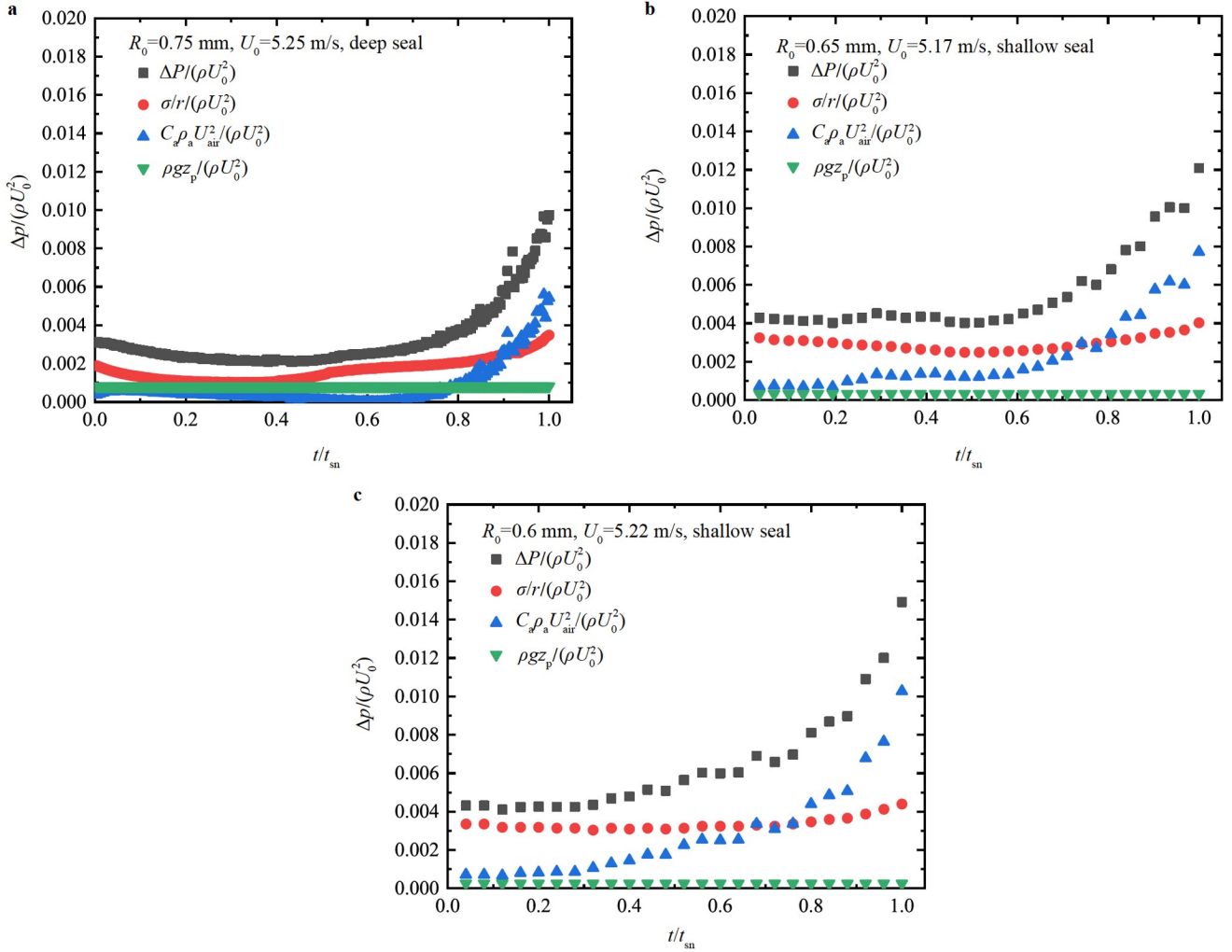
Figure 13 Evolutions of each force and mean total pressure in Eq. (1) at $U_0 \approx 5$ m/s for different radii of the spheres: **a** $R_0 = 0.75$ mm, **b** $R_0 = 0.65$ mm, **c** $R_0 = 0.6$ mm. The pressure difference ΔP and the component forces Δp are nondimensionalized by ρU_0^2. The dotted lines divide the expansion and contraction of the cavities.
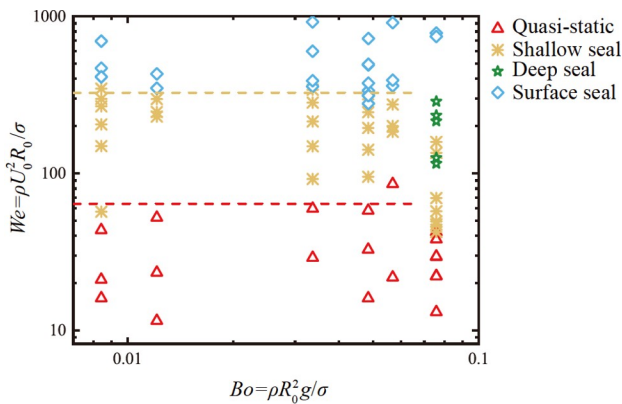

Figure 14 Regime diagram of cavity types induced by the impact of small spheres on the water surface. The ordinate and abscissa are We and Bo, respectively. The ranges of We and Bo are 10-780 and 7.57×10^{-2}–8.41×10^{-3}, respectively. The red triangles, green stars, yellow asterisks, and blue diamonds indicate the regimes of quasi-static, shallow seal, deep seal, and surface seal, respectively.

decreasing Bo. Experiments were conducted based on the laser-driven method to accelerate a small sphere to hundreds of meters per second. A pulse laser was first focused on an aluminum film attached to the reverse side of a water tank cover. A high-pressure plasma was generated, leading to the deformation of the aluminum film and the acceleration of the sphere. In the study, the radius of the sphere R_0 varies from 0.75 mm to 0.25 mm, and the ranges of We and Bo are 10-780 and 7.57×10^{-2}–8.41×10^{-3}, respectively.

Within the Bo range of 1–7.57×10^{-2}, the observations show that cavity types are classified as quasi-static, shallow seal, deep seal, and surface seal. The difference between shallow and deep seals is the position where the cavity first pinches. The cavity seal type transitions from a shallow seal to a deep seal when the pinch-off time of the cross section t_{sn} at the position of the cavity neck increases. t_{sn} increases with the impact velocity U_0 at the same R_0. A high-speed impact leads to a greater amount of momentum being transferred to

the cavity neck so that a larger maximum radius of the cross section is obtained. Furthermore, the pressure difference of the cross section decreases with increasing U_0, which resists the expansion and accelerates the shrinkage of the cavity.

With a further decrease in Bo (5.69×10^{-2}–8.41×10^{-3}), the shallow seal is changed directly to the surface seal, and the deep seal disappears. This is because t_{sn} decreases with a decrease in R_0. The cavity obtains less momentum from the impact of a smaller sphere, resulting in a smaller maximum cavity neck radius. Furthermore, the expansion is resisted, and the shrinkage is accelerated when a larger pressure difference is obtained at lower Bo values. As a result, shallow seals take the place of deep seals. Finally, a parametric study was conducted by varying R_0 and U_0, thus elucidating the influence of We and Bo on the air cavity. Two boundaries are obtained, $We \approx 64$ for the transition between quasi-static and shallow seals and $We \approx 326$ for the transition between shallow and surface seals.

In the future, we will focus on the seal types of water-entry cavity at a smaller Bo than 8.41×10^{-3}. Our previous experiments have found that the deep seal can occur again with the decrease of Bo, but the mechanism needs to be further studied. We plan to investigate the cavity dynamics through a combination of the PIV, optical observation, and numerical simulation.

1   W. Johnson, The ricochet of spinning and non-spinning spherical projectiles, mainly from water. Part II: An outline of theory and warlike applications, Int. J. Impact Eng. **21**, 25 (1998).

2   T. T. Truscott, Cavity Dynamics of Water Entry for Spheres and Ballistic Projectiles, Dissertation for Doctoral Degree, (Massachusetts Institute of Technology, Cambridge, 2009).

3   C. M. Seddon, and M. Moatamedi, Review of water entry with applications to aerospace structures, Int. J. Impact Eng. **32**, 1045 (2006).

4   S. Abrate, Hull slamming, Appl. Mech. Rev. **64**, 060803 (2011).

5   J. W. M. Bush, and D. L. Hu, Walking on water: Biolocomotion at the interface, Annu. Rev. Fluid Mech. **38**, 339 (2006).

6   J. W. M. Bush, D. L. Hu, and M. Prakash, The integument of water-walking arthropods: Form and function, Adv. Insect Physiol. **34**, 117 (2007).

7   J. W. Glasheen, and T. A. McMahon, Vertical water entry of disks at low Froude numbers, Phys. Fluids **8**, 2078 (1996).

8   M. Lee, R. G. Longoria, and D. E. Wilson, Cavity dynamics in high-speed water entry, Phys. Fluids **9**, 540 (1997).

9   R. Bergmann, D. van der Meer, M. Stijnman, M. Sandtke, A. Prosperetti, and D. Lohse, Giant bubble pinch-off, Phys. Rev. Lett. **96**, 154505 (2006).

10   V. Duclaux, F. Caillé, C. Duez, C. Ybert, L. Bocquet, and C. Clanet, Dynamics of transient cavities, J. Fluid Mech. **591**, 1 (2007).

11   T. Grumstrup, J. B. Keller, and A. Belmonte, Cavity ripples observed during the impact of solid objects into liquids, Phys. Rev. Lett. **99**, 114502 (2007).

12   S. Gekle, A. van der Bos, R. Bergmann, D. van der Meer, and D. Lohse, Noncontinuous Froude number scaling for the closure depth of a cylindrical cavity, Phys. Rev. Lett. **100**, 084502 (2008).

13   T. T. Truscott, and A. H. Techet, Water entry of spinning spheres, J. Fluid Mech. **625**, 135 (2009).

14   J. M. Aristoff, T. T. Truscott, A. H. Techet, and J. W. M. Bush, The water entry of decelerating spheres, Phys. Fluids **22**, 032102 (2010).

15   Y. Jiang, T. Bai, Y. Gao, and L. Guan, Water entry of a constraint posture body under different entry angles and ventilation rates, Ocean Eng. **153**, 53 (2018).

16   Q. Yang, F. Xu, Y. Yang, J. Wang, A. Wang, and C. Ma, Numerical study on the dynamic characteristics of water entry of cavity body using two-phase SPH method, Acta Mech. Sin. **37**, 1072 (2021).

17   D. Vella, and P. D. Metcalfe, Surface tension dominated impact, Phys. Fluids **19**, 072108 (2007).

18   D. G. Lee, and H. Y. Kim, Impact of a superhydrophobic sphere onto water, Langmuir **24**, 142 (2008).

19   J. Xie, C. Li, T. Yang, Z. Fu, and R. Li, The motion behavior of micron fly-ash particles impacting on the liquid surface, ACS Omega **7**, 29813 (2022).

20   H. Li, H. Chen, E. Q. Li, C. Y. Zhang, and H. Ding, Impact of superhydrophobic sphere onto a pool covered by oil layer, Phys. Fluids **34**, 032111 (2022).

21   C. Duez, C. Ybert, C. Clanet, and L. Bocquet, Making a splash with water repellency, Nat. Phys. **3**, 180 (2007).

22   J. M. Aristoff, and J. W. M. Bush, Water entry of small hydrophobic spheres, J. Fluid Mech. **619**, 45 (2009).

23   H. Li, S. S. Ji, X. Tan, Z. Li, Y. Xiang, P. Lv, and H. Duan, Effect of Reynolds number on drag reduction in turbulent boundary layer flow over liquid-gas interface, Phys. Fluids **32**, 122111 (2020).

24   H. Ding, B. Q. Chen, H. R. Liu, C. Y. Zhang, P. Gao, and X. Y. Lu, On the contact-line pinning in cavity formation during solid–liquid impact, J. Fluid Mech. **783**, 504 (2015).

25   C. Huang, X. Wen, and M. Liu, Study on low-speed water entry of super-hydrophobic small spheres, Chin. J. Theor. Appl. Mech. **51**, 36 (2019).

26   K. Choi, N. Kim, G. Seon, W. Hwang, and H. Park, Laser-induced control of a cavity bubble behind a sinking sphere in water entry: Dependency on the surface temperature and impact velocity, Phys. Fluids **31**, 122105 (2019).

27   S. D. Guleria, A. Dhar, and D. V. Patil, Experimental insights on the water entry of hydrophobic sphere, Phys. Fluids **33**, 102109 (2021).

28   H. S. Yoo, H. Y. Choi, T. H. Kim, and E. S. Kim, Effect of wettability on the water entry of spherical projectiles: Numerical analysis using smoothed particle hydrodynamics, AIP Adv. **12**, 035014 (2022).

29   H. Li, Z. Li, X. Tan, X. Wang, S. Huang, Y. Xiang, P. Lv, and H. Duan, Three-dimensional backflow at liquid-gas interface induced

by surfactant, J. Fluid Mech. **899**, A8 (2020).

30　J. Eshraghi, S. Jung, and P. P. Vlachos, To seal or not to seal: The closure dynamics of a splash curtain, Phys. Rev. Fluids **5**, 104001 (2020).

随着邦德数减小球体入水空泡闭合类型的探究

钟玉雪, 杜岩, 丘润荻, 肖志坚, 黄荐, 王志英, 王静竹, 王一伟

摘要　入水空泡的演化在自然界和工程领域中出现了有趣的动态现象. 由于很难推动一个小球高速撞击水面, 因此空泡的演化和闭合类型在Bo小于10^{-2}时仍未得到解决. 在本研究中, 进行了一个基于激光驱动原理的实验, 可将小球体加速到数百米每秒. 在$1\sim7.57\times10^{-2}$的Bo范围内, 空泡闭合类型可分为准静态、浅闭合、深闭合和表面闭合. 通过分析空泡颈部的横截面特征, 研究了从浅闭合到深闭合的过渡机制. 随着Bo值的进一步降低($5.69\times10^{-2}\sim8.41\times10^{-3}$), 浅闭合直接转变为表面闭合, 因为颈部横截面的夹断时间随着Bo值的降低而降低, 因此, 深闭合消失了. 最后, 通过改变We和Bo进行参数研究, 得到了两个边界. $We\approx64$是准静态和浅闭合之间的过渡, $We\approx326$是浅闭合和表面闭合之间的过渡.